





## Second harmonic generation on excitons in ZnO/(Zn,Mg)O quantum wells with built-in electric fields

Johannes Mund <sup>1,\*</sup>, Dmitri R. Yakovlev <sup>1,2</sup>, Sergey Sadofev <sup>3</sup>, Cedrik Meier,<sup>4</sup> and Manfred Bayer <sup>1,2</sup>

<sup>1</sup>*Experimentelle Physik 2, Technische Universität Dortmund, D-44221 Dortmund, Germany*

<sup>2</sup>*Ioffe Institute, Russian Academy of Sciences, 194021 St. Petersburg, Russia*

<sup>3</sup>*AG Photonik, Institut für Physik, Humboldt-Universität zu Berlin, D-12489 Berlin, Germany*

<sup>4</sup>*Department Physik, Universität Paderborn, 33095 Paderborn, Germany*



(Received 2 November 2020; revised 23 March 2021; accepted 4 May 2021; published 18 May 2021)

Optical second harmonic generation (SHG) on excitons is studied in polar ZnO/(Zn,Mg)O quantum wells grown on ZnO and sapphire substrates. We observe SHG signal on exciton resonances in a symmetry-forbidden geometry for light propagation along the  $c$  axis of the structure. A symmetry analysis allows us to suggest that the signals are induced by a symmetry reduction with respect to ZnO bulk crystals by the well-barrier interfaces in combination with built-in electric fields due to spontaneous and piezoelectric polarization as well as structural defects.

DOI: [10.1103/PhysRevB.103.195311](https://doi.org/10.1103/PhysRevB.103.195311)

### I. INTRODUCTION

Nonlinear optical spectroscopy using second harmonic generation (SHG) has been established as a powerful tool for exciton spectroscopy of semiconductors [1,2]. In these studies, the laser is tuned to a frequency  $\omega$  in the transparency range of a semiconductor such that the double frequency  $2\omega$  is in resonance with exciton states. The SHG is resonantly enhanced at the exciton resonances and, under application of external electric or magnetic fields, may be seen for crystal orientations, where it is otherwise symmetry forbidden. Analysis of the polarization properties delivers rich information on the symmetry of exciton wave functions and their modifications in external fields, e.g., caused by mixing of different exciton states [3]. One can also access exciton states that are not optically active for one photon absorption or emission and, therefore, cannot be addressed by linear optical spectroscopy. Several bulk semiconductors were studied so far: GaAs, CdTe, ZnSe, ZnO, Cu<sub>2</sub>O, (Cd,Mn)Te, EuTe, and EuSe. Mechanisms of optical harmonic generation, specific for excitons and exciton-polaritons, were disclosed, and the microscopic origins of these mechanisms were considered [3–10].

SHG exciton spectroscopy was used for investigation of two-dimensional semiconductors MoS<sub>2</sub> and WSe<sub>2</sub> [11–13] and quasi-two-dimensional excitons in ZnSe/BeTe quantum wells (QWs) [2,14]. In this paper, we address ZnO/(Zn,Mg)O QWs with built-in electric fields caused by the epitaxial growth on polar ZnO or  $c$ - and  $a$ -plane oriented sapphire substrates. The electric field is induced by both spontaneous and piezoelectric polarizations [15,16].

ZnO is one of the model materials for exciton spectroscopy. It has a large exciton binding energy of 60 meV and shows

pronounced exciton-polariton effects. An overview of its optical properties can be found in Refs. [17,18]. A detailed SHG study of excitons in bulk ZnO can be found in Refs. [3,19], where various magnetic-field-induced SHG mechanisms were analyzed and demonstrated, including the magneto-Stark effect on an exciton moving perpendicular to the magnetic field. SHG was reported for ZnO microcrystals [20], nanocrystals [21], microwires [22], nanowires [23–26], and nanorods [27–32]; for an overview, see Ref. [33]. However, these studies are related to nonresonant SHG and do not address exciton states.

In this paper, we study SHG in the spectral range of the exciton states in polar ZnO/Zn<sub>0.9</sub>Mg<sub>0.1</sub>O QWs, grown on ZnO or  $c$ - and  $a$ -plane sapphire substrates. SHG on the exciton resonances is observed in a symmetry-forbidden geometry. This is explained by symmetry reductions due to the well-barrier interfaces as well as built-in electric fields by internal strain and structural defects.

The paper is organized as follows. In Sec. II, details of the studied samples and experimental techniques are given. Experimental data on SHG are presented in Sec. III. A model analysis is given in Sec. IV, together with comparison with the experimental data. Finally, we discuss the results in Sec. V.

### II. EXPERIMENTAL DETAILS

In this section, we first give the parameters of the samples under study and photoluminescence (PL) spectra for their characterization. Secondly, the experimental setup for the SHG studies is described.

#### A. Samples

A set of high-quality ZnO/Zn<sub>0.9</sub>Mg<sub>0.1</sub>O multiple QWs (MQWs) with the polar  $c$  axis of the structure parallel to the growth direction was used for the SHG studies. The

\*johannes.mund@tu-dortmund.de

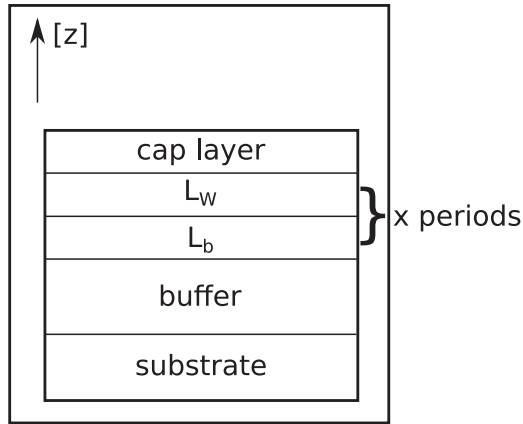


FIG. 1. Schematic diagram of the multiple quantum well (MQW) samples with different layers. Values for the layers of different samples are given in Table I.

samples were grown by plasma-assisted molecular-beam epitaxy (MBE) on either ZnO or sapphire substrates with (0001) orientations. One sample with a QW width of 4.5 nm was grown on an *a*-plane sapphire substrate, but the *c* axis of the MQWs was also parallel to the structure growth axis, i.e., the *c* axes of substrate and MQWs were perpendicular to each other. This is due to the fact that, at room temperature, the long axis of the substrate matches four unit cells of the epilayers basal plane. At low temperatures, the different thermal expansion coefficients of the *a* and *c* axes of the substrate introduce anisotropic strain to the layers [34]. The QW width  $L_w$  varied from 1.8 to 10 nm. The barrier thickness  $L_b$  varied from 8 to 15.3 nm, which is sufficiently large to prevent electronic coupling between neighboring QWs. A schematic diagram of the layers of the sample is given in Fig. 1. The parameters of the MQW samples are given in Table I.

Sample #1 was grown by MBE using an rf-plasma cell for the generation of oxygen radicals. A ZnO single crystal in (0001) orientation (O polar) was used as a substrate. After an

oxygen termination at  $T_S = 700^\circ\text{C}$  for 15 min, a thick ZnO buffer of about 1200 nm was deposited at  $T_S = 700^\circ\text{C}$ , followed by a  $\text{Zn}_{0.9}\text{Mg}_{0.1}\text{O}$  layer of 260 nm deposited at  $450^\circ\text{C}$ . Thereafter, four periods of heterostructure were deposited, consisting of 15.3 nm  $\text{Zn}_{0.9}\text{Mg}_{0.1}\text{O}$  barriers and 1.8-nm-thick ZnO QWs. The top  $\text{Zn}_{0.9}\text{Mg}_{0.1}\text{O}$  barrier was 53 nm thick, serving as a capping layer.

The samples #2 to #5 were grown on *c*-plane sapphire substrates. The growth was initiated by a 2-nm-thick MgO layer deposited at a substrate temperature of  $T_S = 700^\circ\text{C}$ . Next, a 1-nm-thick ZnO and a 40-nm-thick  $\text{Zn}_{0.9}\text{Mg}_{0.1}\text{O}$  layer were grown atop at  $T_S = 360^\circ\text{C}$ . The composite nucleation layer was annealed for 10 min at  $T_A = 730^\circ\text{C}$  to smoothen the surface. The subsequent  $\text{Zn}_{0.9}\text{Mg}_{0.1}\text{O}$  buffer layer of 593–770 nm thickness and the MQWs were grown again at  $T_S = 360^\circ\text{C}$ . The MQWs consisted of either 10 well-barrier periods (samples #3 to #5) or 20 such periods (sample #2). The QW width was varied for the different samples from 2.9 to 10 nm, see Table I. The MQW structure was overgrown by a 22 nm cap  $\text{Zn}_{0.9}\text{Mg}_{0.1}\text{O}$  layer to minimize surface effects. Finally, an annealing step for 3 min at  $700^\circ\text{C}$  was applied to the complete structure. The use of this growth recipe provided high-quality ZnO/ $\text{Zn}_{0.9}\text{Mg}_{0.1}\text{O}$  MQW structures with abrupt flat interfaces. Information on the optical properties of ZnO/(Zn,Mg)O QWs grown by the same recipe can be found in Refs. [35–37].

ZnO crystallizes in the hexagonal wurtzite structure with the point group  $C_{6v}$  ( $6mm$ ). Its band structure is shown in Fig. 2(a). The conduction band (CB) has  $\Gamma_7$  symmetry. The valence band (VB) is split into three bands, denoted by A ( $\Gamma_7$ ), B ( $\Gamma_9$ ), and C ( $\Gamma_7$ ). Their energetic order is still a subject of discussion. Here, the “inverted” order is presented, which was recently confirmed by detailed magneto-optical studies of bulk ZnO [38] and ZnO/(Zn,Mg)O QWs [35]. The band gap between CB and A VB is  $E_g^{\text{ZnO}} = 3.441\text{ eV}$  at the temperature  $T = 6\text{ K}$  [39]. The energy splitting difference between the A and B bands is in the range of 5.6–6.5 meV and between the A and C bands of  $\sim 47\text{ meV}$  [40,41]. The exciton binding energies are similar for the A, B, and C bands

TABLE I. Parameters of the studied ZnO/ $\text{Zn}_{0.9}\text{Mg}_{0.1}\text{O}$  QW samples. Given are the sample number (No.), the well width  $L_w$ , the barrier width  $L_b$ , the number of periods, the thickness of the  $\text{Zn}_{0.9}\text{Mg}_{0.1}\text{O}$  buffer layer, the substrate material, capping layer thickness, and the technological identity code. The emission energies of the exciton  $X_{\text{AB}}$ -resonance measured at  $T = 5\text{ K}$  are given in the row labeled PL. The resonance energies in the SHG spectra are given for the  $X^-$ ,  $X_{\text{AB}}$ , and  $X_{\text{C}}$  state in the rows below.

No.	#1	#2	#3	#4	#5	#6
$L_w$ (nm)	1.8	2.9	3.2	4.5	10	4.5
$L_b$ (nm)	15.3	7.2	8	8	8	8
Periods	4	20	10	10	10	10
Buffer (nm)	676	593	660	690	770	695
Substrate material	ZnO	Sapphire	Sapphire	Sapphire	Sapphire	Sapphire
Substrate orientation	(0001)	<i>c</i> plane	<i>c</i> plane	<i>c</i> plane	<i>c</i> plane	<i>a</i> plane
Substrate thickness ( $\mu\text{m}$ )	500	500	500	500	500	530
Cap layer (nm)	20.6	22	22	22	22	22
Code	133	2262	2182	2183	2187	2190
PL (eV)	3.4521	3.4083	3.3977	3.3797	3.3579	3.3856
$X^-$ (eV)	–	3.4066	3.3968	3.3769	–	3.3787
$X_{\text{AB}}$ (eV)	–	3.4320	3.4136	3.3921	–	3.3940
$X_{\text{C}}$ (eV)	–	–	3.4608	3.4301	–	–

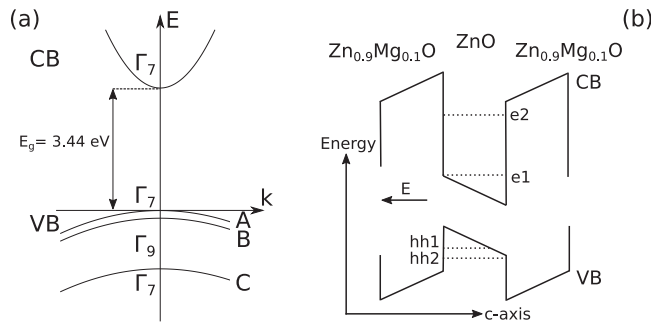


FIG. 2. (a) Band diagram and irreducible representations of ZnO with  $C_{6v}$  symmetry. (b) Band structure of (0001)-oriented ZnO/(Zn,Mg)O multiple quantum wells (MQWs) with built-in electric field  $E$ .  $e1$  and  $e2$  are the electron quantum confined levels, and  $hh1$  and  $hh2$  are the heavy-hole confined levels.

amounting to  $\sim 60$  meV [40], and the exciton Bohr radius is  $a_B = 1.8$  nm.

The band gap of ZnO increases with adding magnesium ions [42], which allows one to use (Zn,Mg)O as a barrier material for ZnO/(Zn,Mg)O QWs. These QWs have a type-I band alignment, where both electrons and holes have their energy minimum in the ZnO wells, see Fig. 2(b). The low-temperature PL of the Zn<sub>0.9</sub>Mg<sub>0.1</sub>O barriers was reported to be located at  $\sim 3.6$  eV energy [43–45]. Considering the exciton binding energy of 60 meV, the barrier band gap is  $\sim 3.66$  eV. Initially, the target of the growth process of our samples #2 to #5 was to exhibit barrier PL at 3.55 eV photon energy.

The distribution of the band gap difference of 220 meV between the CBs and VBs of the well and barrier materials is still an open question for ZnO/(Zn,Mg)O QWs. CB/VB offset ranging between 60/40 and 70/30 were proposed [46], and the ratio of 65/35 was used for calculations [47]. This ratio between CB and VB would result in respective band offsets of 143 and 77 meV.

An interesting property of ZnO/(Zn,Mg)O QWs grown on the polar  $c$  plane is the presence of a built-in electric field  $E$  oriented along the  $c$  axis, which is the growth axis of the structure. The electric field is induced by spontaneous polarization and by the piezoelectric effect caused by the lattice mismatch between the QW and barrier materials [15,48,49]. It was shown in Ref. [16] that the built-in electric field in ZnO/(Zn,Mg)O QWs with thick barriers varies linearly with magnesium composition  $x$  and amounts to  $\sim 0.3$  MVcm<sup>-1</sup> for  $x = 0.1$ . However, the built-in field as a combination of spontaneous and piezopolarization also depends on the crystal polarity (O or Zn), the structure design, and the sample temperature [50]. The effect of the electric field on the confinement potential of the QW structure is schematically shown in Fig. 2(b).

The exciton states are influenced by the built-in electric field, as electrons and holes are separated toward the opposite interfaces of the QW. Thus, the exciton oscillator strength is reduced and, vice versa, its lifetime is extended. Also, the exciton resonance is shifted to lower energies due to the effective band gap reduction, even though the exciton binding energy is reduced by the field. This shift is small in QWs thinner than 4 nm but becomes significant in wider QWs. For example, for

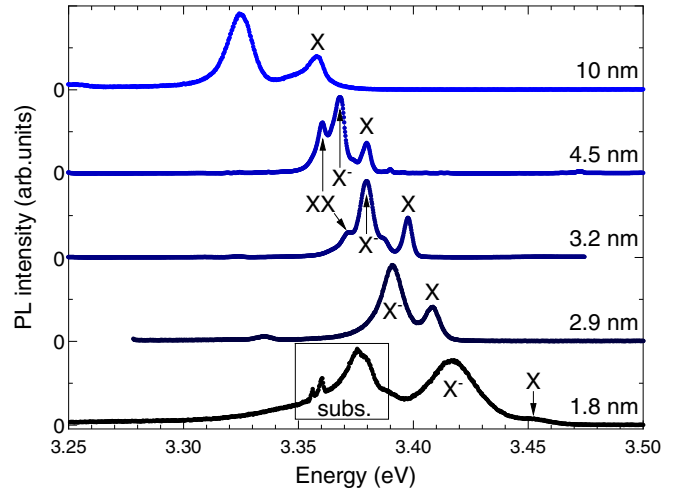


FIG. 3. Photoluminescence (PL) spectra of ZnO/Zn<sub>0.9</sub>Mg<sub>0.1</sub>O multiple quantum wells (MQWs) with well widths varying from 1.8 to 10 nm. The exciton (X), negatively charged trion (X<sup>-</sup>), and biexciton (XX) lines are marked by arrows  $T = 5$  K.

the 10 nm QW, it results in the exciton energy being below the exciton energy in bulk ZnO [16,48,51]. The built-in electric field can be screened by photogenerated carriers of high density, which results in a shift to higher energies of the exciton emission line [51]. In the periodic QW structures, the built-in electric field in the QW is reduced by a factor of  $L_b/(L_w + L_b)$  [52]. An overview of the optical properties of excitons in ZnO/(Zn,Mg)O QWs can be found in Refs. [35–37,53–55].

## B. PL spectra

To characterize the samples under study, we measured their PL at the temperature of  $T = 5$  K, see Fig. 3. The excitation was provided by a pulsed laser (3.3 ps pulse duration, repetition frequency of 30 kHz), where a photon energy of 1.906 eV was doubled to 3.812 eV by a  $\beta$ -barium borate (BBO) crystal. The laser was focused on a spot with the diameter of  $\sim 0.5$  mm, and an average power of 1 mW was used.

For the identification of the PL lines shown in Fig. 3, we rely on Refs. [35–37,55]. Three types of exciton complexes are seen: neutral excitons (X), which are localized on the well width fluctuations, negatively charged excitons (trions X<sup>-</sup>) consisting of two electrons and one hole, and biexcitons (XX). The exciton resonances shift with decreasing QW width from 3.358 eV in the 10 nm QWs to 3.452 eV in the 1.8 nm QWs. Its energy is contributed by quantum confinement and the built-in electric field, which induce shifts in opposite directions. In sample #1, grown on a ZnO substrate, one can see the substrate PL in the spectral range of 3.33–3.39 eV. Note that the resonance energy of the 1S state of the A exciton in bulk ZnO is 3.3759 eV [56]. The ZnO emission is not present in other samples, as they were grown on sapphire substrates. The exciton lines have rather small linewidths [full widths at half maximum (FWHMs)] of  $\sim 5$  meV in the QWs of 2.9, 3.2, and 4.5 nm width, which confirms the high structural quality of these samples. The line broadens in the 1.8 nm QWs to 18 meV due to the stronger exciton localization on well width

fluctuations. The line is also broadened to 14 meV in the 10 nm QWs, where the localization is provided by the built-in electric field.

The trion emission line is shifted from the exciton line by 36, 17.8, 18.3, and 11.4 meV, for QW widths of 1.8, 2.9, 3.2, and 4.5 nm, respectively. These values are in agreement with the trion binding energy of 13 meV reported for 3.5 nm ZnO/Zn<sub>0.91</sub>Mg<sub>0.09</sub>O MQWs [35]. The biexciton lines observed in the 3.2 and 4.5 nm wells are shifted, respectively, by 26.6 and 19.4 meV from the exciton line. The reported biexciton binding energy in 3.5 nm ZnO/Zn<sub>0.91</sub>Mg<sub>0.09</sub>O MQWs is 19 meV [35], and in 3.7 nm and 1.75 nm ZnO/Zn<sub>0.74</sub>Mg<sub>0.26</sub>O MQWs, it is 19 and 28 meV, respectively [57]. The biexciton binding energy in bulk ZnO is 15 meV [58].

### C. SHG experimental technique

Optical SHG spectra were measured by exciting the sample with laser pulses of 3.3 ps duration and a FWHM of  $\sim 1$  meV. The photon energy of the laser light was scanned in the ZnO transparency range around about half of the band gap energy from 1.58 to 1.80 eV (690–785 nm). The pulses were emitted at a rate of 30 kHz by a tunable ps-optical parametric amplifier (OPA). The OPA was pumped by two trains of laser pulses, namely, 150 fs laser pulses at 1030 nm and 3.3 ps pulses at 515 nm provided by a second harmonic bandwidth compressor. The energy per pulse was set to 0.7  $\mu$ J.

The laser beam hit the ZnO-MQW sample surface at an angle  $\theta$  between the light direction  $\mathbf{k}^\omega$  and the [0001] crystal  $c$  axis. For  $\theta = 0^\circ$ , the light direction is parallel to the  $c$  axis and enters the crystal under normal incidence. Note that  $\theta$  is taken as the angle inside of the samples which already accounts for the refractive index of ZnO [59]. Sample tilting about the horizontal laboratory axis  $[2\bar{1}\bar{1}0]$  was minimized by adjustment to the back reflection. A possible misalignment was further reduced by the refractive index of the sample. We estimate the misalignment to  $\leq 2^\circ$ . The light was focused into a spot with size of  $\sim 100$   $\mu$ m. The measurements were performed in transmission geometry. The samples were excited from the substrate side to avoid possible reabsorption of the SHG signal, e.g., in the ZnO substrate. In Fig. 4, the sample orientation relative to the optical axis as well as the linear polarization angles of the fundamental and second harmonic light are specified.

With two sets of Glan-Thompson polarizer and a half-wave plate, (1) the linear polarization of the incoming light can be varied continuously, and (2) a certain polarization of the outgoing light is projected independently. One can thus detect the signals for any linear polarization configuration of  $\mathbf{E}^\omega$  or  $\mathbf{E}^{2\omega}$  and, therefore, measure the rotational anisotropy diagrams of the optical harmonics. In this paper, we measure these anisotropies for either parallel ( $\mathbf{E}^\omega \parallel \mathbf{E}^{2\omega}$ ) or crossed ( $\mathbf{E}^\omega \perp \mathbf{E}^{2\omega}$ ) linear polarizations of the laser and signal light.

The SHG signals were detected by the combination of a spectrometer and a silicon charge-coupled device (CCD) camera (matrix with  $1340 \times 400$  pixels, pixel size 20  $\mu$ m), cooled by liquid nitrogen. A 0.5 m focal length monochromator (Acton, Roper Scientific) with a 1800 grooves/mm grating was used. The overall spectral resolution of the system was 200  $\mu$ eV, contributed by the spectral width of the laser and

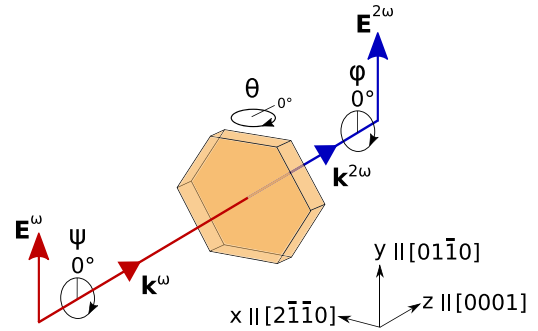


FIG. 4. Sample orientation relative to the optical axis and linear polarization angles in the second harmonic generation experiments. The ingoing light with frequency  $\omega$  and electric field  $\mathbf{E}^\omega$  has the wave vector  $\mathbf{k}^\omega$  with a polarization angle  $\psi$ . The generated harmonic light with frequency  $2\omega$  and electric field component  $\mathbf{E}^{2\omega}$  has the wave vector  $\mathbf{k}^{2\omega}$  and is detected at a polarization angle  $\phi$ . The internal angle between  $\mathbf{k}^\omega$  and the [0001] axis is given by  $\theta$ .

the spectral resolution of the detection system. This was the value by which the laser photon energy was tuned in each measurement step. Furthermore, we did not integrate over the laser line width but integrated over a  $6 \times 6$  pixel area with the second harmonic intensity maximum in its center from the CCD camera. For optical measurements, the sample was kept in a bath cryostat at the temperature of  $T = 5$  K through contact with cold helium gas. External magnetic fields up to 10 T generated by a superconducting solenoid can be applied perpendicular to the light wave vector ( $\mathbf{B} \perp \mathbf{k}^\omega$ ), i.e., in the Voigt geometry.

## III. EXPERIMENTAL RESULTS

In this section, SHG spectra and rotational anisotropies are presented and compared with the PL spectra. Firstly, the sample was rotated around the vertical  $y$  axis, i.e.,  $\mathbf{k}^\omega \nparallel c$  axis. In this geometry, SHG is symmetry allowed, as it was shown for bulk ZnO [1]. In a second step, we aligned the sample surface perpendicular to the laser light ( $\theta = 0^\circ$ ) to suppress any SHG. Still, we find pronounced resonances in the SHG measurements.

### A. SHG in tilted geometry

In Fig. 5(a), the SHG signal recorded in tilted geometry from the 3.2 nm MQWs (black) is compared with the signal which was obtained from a Zn<sub>0.9</sub>Mg<sub>0.1</sub>O epilayer with a thickness of 590 nm (sample code 2261, red). For the MQW sample, several broad resonances are detected in the energy ranges 3.40–3.44 eV and 3.46–3.54 eV. The Zn<sub>0.9</sub>Mg<sub>0.1</sub>O epilayer shows no pronounced resonances in the same range but only a rather featureless signal increasing continuously toward lower energies. Therefore, the resonances can be excluded to originate from the barrier and buffer material in the MQW samples in the studied energy range.

In Fig. 5(b), a rotational anisotropy diagram representative for the whole SHG spectrum of the MQW sample in Fig. 5(a) is plotted. The parallel anisotropy (black dots) has a characteristic shape with a twofold rotational symmetry, while the crossed one (red dots) has a fourfold symmetric shape. These

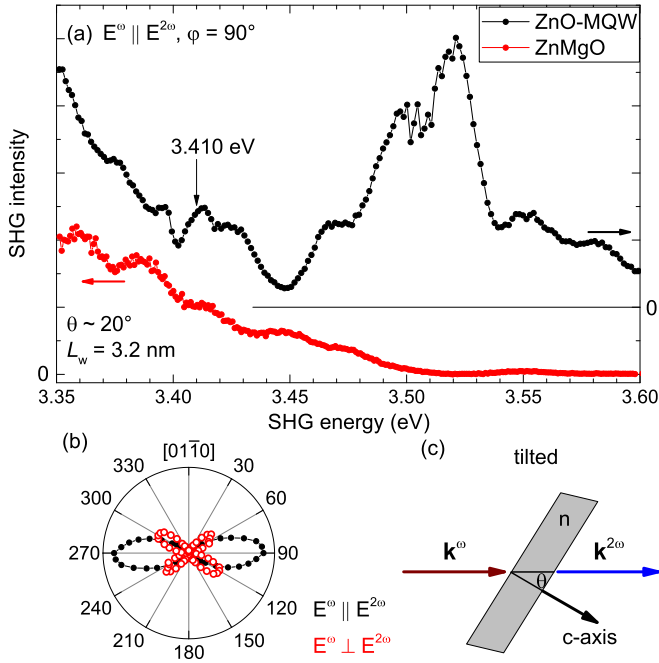


FIG. 5. (a) Second harmonic generation (SHG) spectrum of the multiple quantum well (MQW) sample #3 (3.2 nm, black line) and of the reference  $\text{Zn}_{0.9}\text{Mg}_{0.1}\text{O}$  epilayer (red line), measured for the tilt angle  $\theta = 20^\circ$ . (b) Rotational anisotropy of SHG in the MQW sample measured at 3.410 eV. It is representative for the whole spectral range shown in panel (a). Filled black and open red circles show data for the  $\mathbf{E}^\omega \parallel \mathbf{E}^{2\omega}$  and  $\mathbf{E}^\omega \perp \mathbf{E}^{2\omega}$  configurations, respectively. (c) Schematics of the experimental geometry. The angle between the light wave vector and the structure growth axis ( $c$  axis) inside the sample is  $\theta$ ;  $n$  is the refractive index of the sample.

patterns can be understood by a symmetry analysis which also reveals the material parameters.

The source of the SHG signal in tilted geometry can be the ZnO QWs, but also the  $\text{Zn}_{0.9}\text{Mg}_{0.1}\text{O}$  of the barriers or

$$\begin{aligned}
 I_{\parallel, C_{3v}}^{2\omega} &\propto \{\chi_{xxy} \cos(\varphi) [\cos(\varphi)^2 - 3\cos(\theta)^2 \sin(\varphi)^2] \\
 &\quad + (2\chi_{xxz} + \chi_{zxx}) \sin(\varphi) [\cos(\varphi)^2 + \cos(\theta)^2 \sin(\varphi)^2] \sin(\theta) + \chi_{zzz} \sin(\varphi)^3 \sin(\theta)^3\}^2, \\
 I_{\perp, C_{3v}}^{2\omega} &\propto \{-\chi_{xxy} \cos(\varphi)^2 [2 + \cos(2\theta)] \sin(\varphi) + \chi_{xxy} \cos(\theta)^2 \sin(\varphi)^3 \\
 &\quad + \chi_{zxx} \cos(\varphi)^3 \sin(\theta) + \sin(\varphi)^2 \cos(\varphi) \sin(\theta) [\chi_{zxx} \cos(\theta)^2 + (-2\chi_{xxz} + \chi_{zzz}) \sin(\theta)^2]\}^2.
 \end{aligned} \tag{8}$$

The fits of Eqs. (8) and (9) to the anisotropy in Fig. 5(b) are shown in Fig. 6 along with the fit parameters. Here, for better visibility, Cartesian axes are used for presentation instead of polar axes. It can be deduced from the fit that  $\chi_{zzz}$  is the main active tensor component in the tilted geometry. Note that, for the fit, the tensor components are normalized on the strongest one, in this case, on  $\chi_{zzz} = 1$ . The contribution of  $\chi_{xxz}$  is small, and those of  $\chi_{zxx}$  and  $\chi_{xxy}$  are negligible. Therefore, from these data, we cannot conclude about the symmetry responsible for the SHG signal because the active components are present both in the  $C_{6v}$  and  $C_{3v}$  cases. Furthermore, in tilted geometry,

the 593–770-nm-thick  $\text{Zn}_{0.9}\text{Mg}_{0.1}\text{O}$  buffer layer. In terms of crystal symmetry, the thick buffer layer has  $C_{6v}$  symmetry, just as ZnO bulk material. The symmetry of the wells and barriers is reduced to  $C_{3v}$  because the translational invariance along the  $c$  axis is broken by the interfaces [60]. To model the rotational anisotropy in Fig. 5(b), we consider the two-photon induced nonlinear polarization  $P^{2\omega}$  at twice the fundamental laser frequency  $2\omega$  by

$$P_i^{2\omega} = \epsilon_0 \chi_{ijl} E_j^\omega E_l^\omega, \tag{1}$$

with  $i, j, l$  as Cartesian indices,  $\epsilon_0$  the permittivity of the vacuum,  $\chi_{ijl}$  the nonlinear optical susceptibility, and  $E_{j(l)}^\omega$  the components of the incoming electric field. The allowed, non-vanishing tensor components for  $C_{6v}$  and  $C_{3v}$  symmetry can be found from literature, e.g., see Ref. [61]. These components for  $C_{6v}$  are

$$\chi_{xzx} = \chi_{yzy}, \tag{2}$$

$$\chi_{xxz} = \chi_{yyz}, \tag{3}$$

$$\chi_{zxx} = \chi_{zyy}, \tag{4}$$

$$\chi_{zzz} \tag{5}$$

with the entries  $z$  parallel to the sample growth axis ( $c$  axis). We note that, in our case of frequency-degenerate photons, the components of Eqs. (2) and (3) are equal. The only difference for  $C_{3v}$  is an additional component with no  $z$  entries:

$$\chi_{yyy} = -\chi_{yxx} = -\chi_{xxy} = -\chi_{xyx}. \tag{6}$$

With an incoming electric field of the form

$$E^\omega = \begin{pmatrix} -\sin(\varphi) \cos(\theta) \\ \cos(\varphi) \\ \sin(\varphi) \sin(\theta) \end{pmatrix}, \tag{7}$$

the angular dependencies of the SHG intensity for the parallel ( $I_{\parallel}^{2\omega}$ ) and crossed ( $I_{\perp}^{2\omega}$ ) configurations are given by Eqs. (8) and (9). The full expressions give the result for  $C_{3v}$  symmetry, whereas those for  $C_{6v}$  are obtained by setting  $\chi_{xxy} = 0$ .

the light polarization might be affected by the substrate birefringence of the  $c$  and  $a$  axes. However, we observe no such effect since the anisotropy pattern in Fig. 6 is not distorted and can be fitted by Eqs. (8) and (9), which do not account for birefringence.

## B. SHG at normal light incidence

At normal incidence ( $\theta = 0^\circ$ ), the light wave vector is parallel to the  $c$  axis, and no SHG is expected since the transversely polarized light has no component along the  $c$  axis.

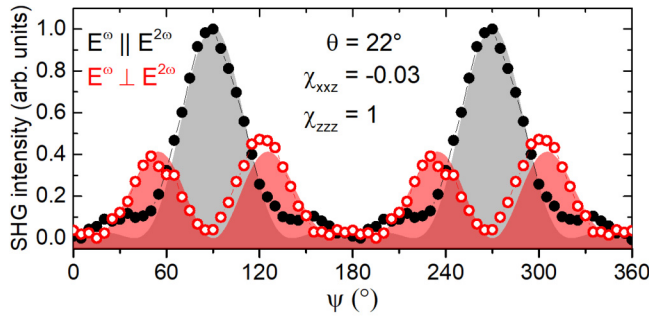


FIG. 6. Second harmonic generation (SHG) anisotropy of the sample #3 (3.2 nm) measured at 3.410 eV photon energy in tilted geometry. The filled black and open red dots present data for the configurations  $\mathbf{E}^\omega \parallel \mathbf{E}^{2\omega}$  and  $\mathbf{E}^\omega \perp \mathbf{E}^{2\omega}$ , respectively. The gray and red shaded areas are the corresponding fits.

However, a SHG signal is still present at normal incidence, as shown for sample #3 with  $L_w = 3.2$  nm in Fig. 7(a). We assign the most intense line labeled  $X_{AB}$  to the 1S excitons of the A and B VBs, which are split by a few millielectronvolts in bulk ZnO [39]. This splitting is not clearly resolved but is evident from the asymmetric shape of the line. The Stokes shift between the SHG and PL exciton lines is 15 meV. The narrow line shifted by 20 meV to lower energies relative to the exciton is assigned to the negatively charged exciton  $X^-$ , as the shift corresponds well to the trion binding energy in PL. The line at 3.46 eV labeled as  $X_C$  is shifted by 40 meV to higher energy relative to the  $X_{AB}$  line, which is close to the energy splitting between the B and C VBs. Thus, we assign this line to the 1S exciton of the C band. It is worthwhile to note that the overall SHG intensity at normal incidence is  $\sim 40$  times smaller than the intensity for the tilted case in Fig. 5(a).

Furthermore, the SHG signal intensity in the low energy range (3.30–3.39 eV) of the normal incidence spectrum is

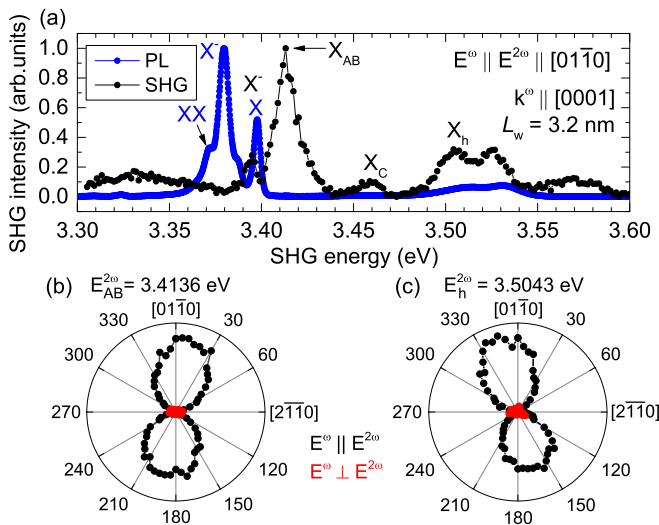


FIG. 7. (a) Comparison of second harmonic generation (SHG) spectrum measured at normal incidence (black) and photoluminescence (PL) spectrum (blue) of the 3.2 nm multiple quantum wells (MQWs; sample #3). SHG rotational anisotropies measured at the energies of (b)  $X_{AB}$  and (c)  $X_h$ .

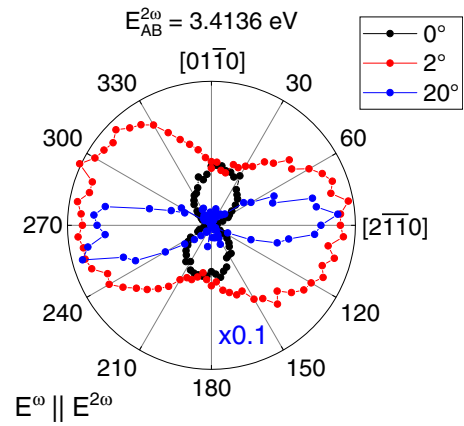


FIG. 8. Parallel rotational anisotropy of the  $X_{AB}$  resonance for internal tilting angles of  $\theta = 0^\circ$  (black),  $2^\circ$  (red), and  $20^\circ$  (blue). Note that the signal intensity for  $\theta = 20^\circ$  is considerably stronger and is reduced by a factor of 10 for better comparison.

drastically reduced. This can be used as an indicator for light incidence parallel to the  $c$  axis, independent of possible misaligned surfaces with respect to the crystal structure. In the PL and SHG spectra, further resonances are present in the energy range of 3.50–3.55 eV. They are at lower energy than expected for the PL signal from the barriers (3.55 eV), although they could represent Stokes-shifted emission from these states. Another possibility could be that these resonances correspond to QW excitons formed from charge carriers at higher confined levels.

In Figs. 7(b) and 7(c), the rotational SHG anisotropies for the resonances  $X_{AB}$  and  $X_h$  are shown. Whereas the rotational SHG anisotropy shape shown in panel (b) is representative for the resonances labeled by  $X^-$ ,  $X_{AB}$ , and  $X_C$ , that in panel (c) is measured at the resonances labeled by  $X_h$  and 3.525 eV. The parallel anisotropy pattern in Fig. 7(b) is directed along the  $[01\bar{1}0]$  crystal axis within the experimental accuracy. The parallel anisotropy in Fig. 7(c) is also collinear to that crystal direction. An analysis of the anisotropies is provided in Sec. IV.

It is instructive to trace the change of the rotational anisotropy patterns from normal incidence to tilted geometry to highlight the contributions of responsible mechanisms inducing the SHG signal. For that, we show in Fig. 8 the parallel anisotropies for internal tilting angles of  $\theta = 0^\circ$ ,  $2^\circ$ , and  $20^\circ$ . For the small tilting angle of  $2^\circ$ , the twofold symmetric anisotropy pattern along the  $[01\bar{1}0]$  crystal axis is superimposed by signal along the  $[2\bar{1}\bar{1}0]$  axis, which is induced by tilting the crystal. At a tilting angle of  $20^\circ$ , the induced signal is  $\sim 10$  times more intense than the original one. Thus, the normal incidence signal is still present, even though it is hidden underneath the signal from the tilting.

SHG spectra of the samples with well widths of 2.9 and 4.5 nm are shown in Figs. 9 and 10, respectively. The most intense SHG resonance is labeled by  $X_{AB}$ . Like the sample with 3.2 nm well width, a less intense line  $X^-$  is present at the low energy side of  $X_{AB}$ . The resonance  $X_C$  is clearly seen in the 4.5 nm sample but absent in the 2.9 nm one, probably due to its broadening. The SHG rotational anisotropies shown in Figs. 9(b) and 9(c) exhibit an intense twofold shape along

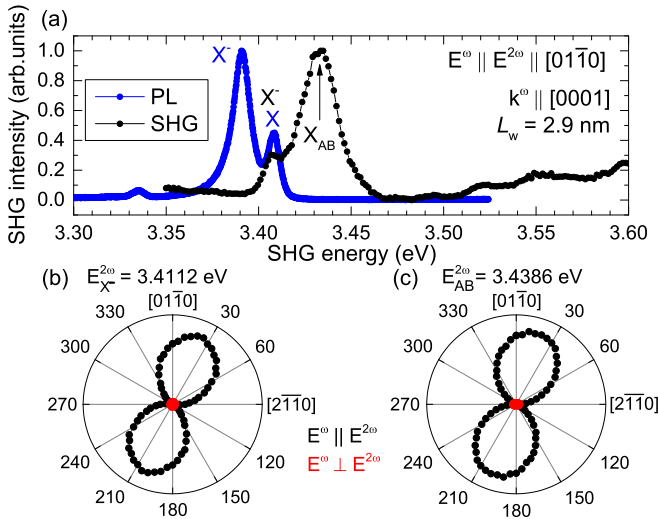


FIG. 9. (a) Comparison of second harmonic generation (SHG) spectrum measured at normal incidence (black) and photoluminescence (PL) spectrum (blue) of the 2.9 nm multiple quantum wells (MQWs; sample #2). SHG rotational anisotropies measured at the energies of (b) X<sup>-</sup> and (c) X<sub>AB</sub>.

20° polarization. Those shapes shown in panels (b) and (c) of Fig. 10 are representatives of the following SHG resonances. The shape of panel (b) is present at X<sup>-</sup>, X<sub>AB</sub>, and at X<sub>C</sub>; that of panel (c) at X<sub>h</sub> and at the resonance at 3.525 eV.

As can be seen in Fig. 11, in the sample with 1.8 nm QWs no SHG signal is detected. We attribute this finding to the low amount of well material for only four thin QWs in this sample. The SHG signal is also very weak in the 10 nm MQWs sample. No clear resonances can be identified in the spectrum. We suggest that the reason for the weak signal is

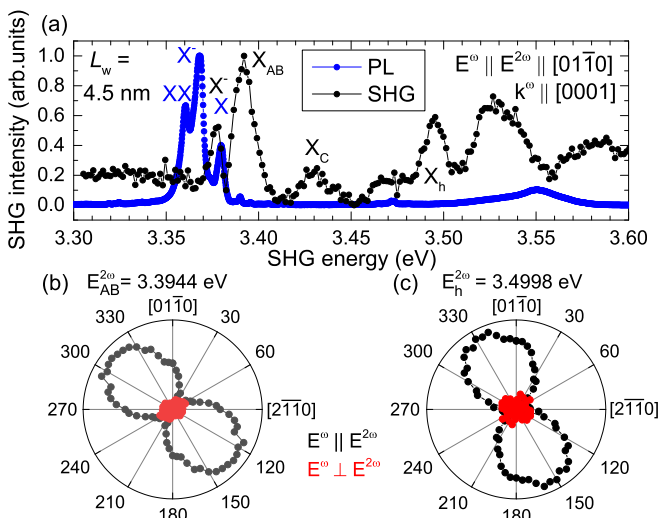


FIG. 10. (a) Comparison of second harmonic generation (SHG) spectrum measured at normal incidence (black) and photoluminescence (PL) spectrum (blue) of the 4.5 nm multiple quantum wells (MQWs; sample #4). SHG rotational anisotropies measured at the energies of (b) X<sub>AB</sub> and (c) X<sub>h</sub>.

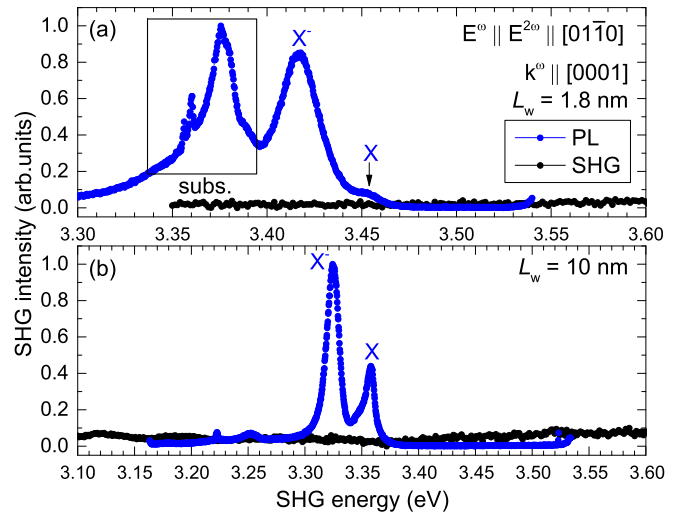


FIG. 11. Comparison of second harmonic generation (SHG) spectra measured at normal incidence (black) and photoluminescence (PL) (blue) spectra for the: (a) 1.8 nm multiple quantum wells (MQWs; sample #1) and (b) 10 nm MQWs (sample #5).

the strong built-in electric field, which reduces the exciton oscillator strength and broadens the exciton line.

The SHG resonance energies in dependence on well width are plotted in Fig. 12 together with the PL peak energies. The values of the peak energies are also listed in Table I.

Strong external magnetic fields, which modify the exciton states by mixing states of different symmetries, are often used to induce SHG signals along symmetry-forbidden geometries [2]. We tested this approach for the studied ZnO/Zn<sub>0.9</sub>Mg<sub>0.1</sub>O MQWs by applying magnetic fields up to 10 T in Voigt

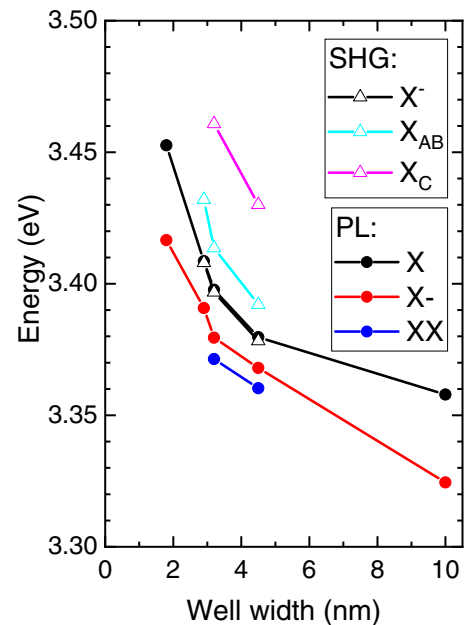


FIG. 12. Summary of the energies of the resonances in the second harmonic generation (SHG) (open triangles) and photoluminescence (PL) (closed circles) spectra for the studied ZnO/Zn<sub>0.9</sub>Mg<sub>0.1</sub>O multiple quantum wells (MQWs).

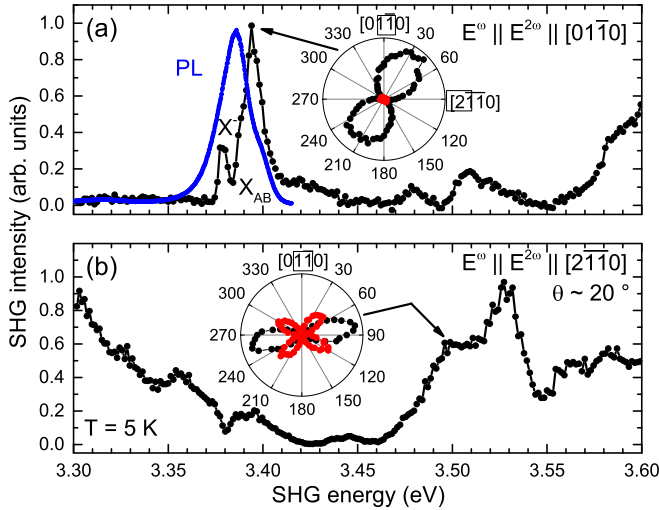


FIG. 13. Second harmonic generation (SHG) spectra of the 10 period 4.5 nm ZnO/Zn<sub>0.9</sub>Mg<sub>0.1</sub>O multiple quantum wells (MQWs) sample (sample #6) grown on an *a*-plane sapphire substrate. The spectra are measured at (a) normal incidence and (b) in tilted geometry  $\theta \sim 20^\circ$ . The insets show rotational anisotropies, where the full black and open red dots correspond to the  $\mathbf{E}^\omega \parallel \mathbf{E}^{2\omega}$  and  $\mathbf{E}^\omega \perp \mathbf{E}^{2\omega}$  configurations, respectively. Photoluminescence (PL) spectrum is shown in panel (a) by a blue line.

geometry ( $\mathbf{B} \perp \mathbf{k}^\omega$ ). Only small changes of the SHG intensity at the exciton resonances were detected. Thus, the magnetic-field-induced signals are weaker than that induced by other mechanisms, tentatively by internal electric fields or interfaces. Particularly, neither do the resonances shift in energy, nor do new resonances appear, as is often the case when SHG becomes allowed by magnetic fields.

The SHG spectra and rotational anisotropies measured at normal light incidence and in tilted geometry for the sample grown on the *a*-plane sapphire substrate are shown in Fig. 13. In this structure, the *c* axis of *a*-plane sapphire is perpendicular to the *c* axis of the ZnO-based heterostructure. No principal SHG differences are found between the *a*-plane and *c*-plane samples in Fig. 10(b) with the same well width of 4.5 nm and barrier concentration of Mg. It is important to note that, in case of the sample grown on the *a*-plane sapphire substrate, the anisotropic in-plane strain is present at cryogenic temperatures [34]. It can decrease the symmetry of the MQW and be the origin of the SHG signal in the otherwise symmetry-forbidden configuration. The different refractive indexes of the substrate *a* and *c* axis might affect the light polarization direction. Still, no pronounced effect is observed in normal incidence. In tilted geometry [Fig. 13(b)], the parallel rotational anisotropy is slightly tilted from the  $90^\circ$  axis. However, this could also be due to a small misalignment of the sample.

#### IV. SYMMETRY ANALYSIS

When the sample is set to normal light incidence ( $\theta = 0^\circ$ ), the ingoing and outgoing photons are polarized in the *xy* plane, i.e., no *z* polarization is present. Therefore, all tensor components in Eqs. (2)–(5) vanish, and only the additional

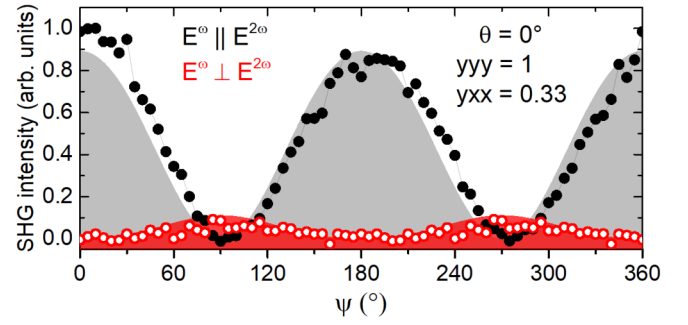


FIG. 14. Comparison of the experimental rotational anisotropy from Fig. 7(b); full black and open red dots give data in the  $\mathbf{E}^\omega \parallel \mathbf{E}^{2\omega}$  and  $\mathbf{E}^\omega \perp \mathbf{E}^{2\omega}$  configuration, respectively. Gray and red shaded areas are fits to the data by Eqs. (10) and (11) using the parameters given in the inset.

component from the  $C_{3v}$  symmetry in Eq. (6) remains. The calculated rotational anisotropy shape is, however, sixfold for both the parallel and crossed configurations, which is not confirmed by the measured SHG signals in Figs. 7(b) and 7(c). Therefore, we have to suggest a further reduction of symmetry to the point group  $C_{1v}$  (*m*). The according simulation is presented in this section, and possible reasons for the symmetry reduction are discussed in the next section.

The tensor components of the point group  $C_{1v}$  are  $\chi_{yyy}$ ,  $\chi_{yxx}$ ,  $\chi_{xyz}$ , and  $\chi_{yzz}$  [62] (note that depending on the actual *xy*-plane sample orientation the indices *x* and *y* are interchangeable), out of which the latter two vanish in the normal incidence geometry. The calculated angle dependencies of the SHG intensity for parallel and crossed intensity are given by

$$I_{\parallel, C_{1v}}^{2\omega} \propto [3\chi_{yxx}\cos(\varphi)^2\sin(\varphi) + \chi_{yyy}\sin(\varphi)^3]^2, \quad (10)$$

$$I_{\perp, C_{1v}}^{2\omega} \propto [\chi_{yxx}\cos(\varphi)^3 + (\chi_{yyy} - 2\chi_{yxx})\cos(\varphi)\sin(\varphi)^2]^2. \quad (11)$$

In Fig. 14, the measured rotational anisotropy from Fig. 7(b) is shown together with the best-fit simulation, giving the parameters  $\chi_{yyy} = 1$  and  $\chi_{yxx} = 0.33$ . The rotational anisotropy in tilted geometry, shown in Fig. 7(c), cannot be simulated by Eqs. (10) and (11), even if a small tilting angle  $\theta$  is introduced, which would allow for the contributions of  $\chi_{xyz}$  and  $\chi_{yzz}$ .

We conclude this section by summarizing that the rotational anisotropy in tilted geometry can only be simulated by the point groups  $C_{6v}$  or  $C_{3v}$  but not by  $C_{1v}$ . In contrast, the rotational anisotropy at normal incidence of light can only be achieved by assuming the symmetry of the point group  $C_{1v}$ . Possible reasons for the symmetry reduction are discussed in the next section.

#### V. DISCUSSION

The symmetry reduction from  $C_{6v}$  to  $C_{3v}$ , when going from a bulk crystal to two-dimensional QWs, is straightforward to explain by the broken translational invariance along the *c* axis. However, a further reduction to  $C_{1v}$ , which produces the twofold symmetry axis as seen in Fig. 7(b), can have several origins.



We studied a sample grown on an  $a$ -plane substrate, Fig. 13, to address the possibility of internal anisotropic strain. This strain originates from different thermal expansion coefficients of the  $a$  and  $c$  axes of the sapphire substrate, which strain the ZnO QW layers at cryogenic temperatures. However, by comparing the spectra and rotational anisotropies in Fig. 7 ( $c$ -plane sapphire) and Fig. 13 ( $a$ -plane sapphire), no fundamental difference can be found. In both cases, a pronounced twofold anisotropy shape is present for the  $X_{AB}$  exciton. The built-in strain in the samples grown on  $c$ -plane sapphire is expected to be smaller, whereas our experimental data show that it can be the origin of a SHG signal in the symmetry-forbidden geometry.

Another reason for a breaking of symmetry would be a tilt induced by the growth process. The orientation of the sapphire wafers (CrysTec GmbH) is specified with a tolerance of  $0.3\text{--}0.5^\circ$ . During epitaxial growth an additional tilt with respect to the basal substrate plane may be introduced. However, this effect is expected to be relatively small to explain the observed anisotropy alone. Twin boundaries can also arise in the growth process [62,63] and induce an in-plane anisotropy.

ZnO/(Zn,Mg)O MQWs are known to exhibit an internal electric field parallel to the  $c$  axis due to spontaneous and piezoelectric polarization [15,16]. From the point of symmetry, such a field does not further reduce the point group  $C_{3v}$  of the QW structure. However, interfaces (even ideal) have lower symmetry than their host materials, as they are formed by the chemical bonds between specific elements. In symmetric QWs, where the exciton wave function has equal density on both opposite interfaces, this difference is averaged. However, in the case when the exciton is pushed closer to one of the interfaces, as it can happen in ZnO-based QWs due to piezoelectric effect, this difference becomes important and

may cause an additional symmetry reduction for the exciton state. Still, in the hexagonal ZnO structure, one would expect a threefold or sixfold symmetry instead of the observed twofold one. The spatial separation of electrons and holes results in decreasing exciton oscillator strength, particularly for broad QWs. In addition, such an electric field could also have in-plane components and thus reduce the symmetry of the excitons, which would induce the SHG signals with the rotational anisotropies that we have found experimentally.

## VI. CONCLUSIONS

In conclusion, we have reported on the experimental observation of SHG signals at the exciton and trion resonances in ZnO/Zn<sub>0.9</sub>Mg<sub>0.1</sub>O MQWs with well thicknesses of 1.8–10 nm. Surprisingly, the SHG exciton resonances are found even for the light incident parallel to the growth  $c$  axis of the samples, which is a symmetry-forbidden geometry for SHG. However, the symmetry of the MQWs is reduced by their interfaces and possibly by internal strain or growth defects. The simulation of rotational anisotropies at normal incidence and in tilted geometry reveals that the SHG has two sources of different symmetry, which can be addressed independently by setting the light polarization accordingly.

## ACKNOWLEDGMENTS

The authors are thankful to D. Fröhlich, M. M. Glazov, M. A. Semina, A. V. Rodina, E. L. Ivchenko, J. Puls, T. V. Shubina, and A. A. Toropov for helpful discussions. We acknowledge the financial support by the Deutsche Forschungsgemeinschaft through the Collaborative Research Centre TRR 142 (Project B01).

- 
- [1] R. V. Pisarev, B. Kaminski, M. Lafrentz, V. V. Pavlov, D. R. Yakovlev, and M. Bayer, Novel mechanisms of optical harmonics generation in semiconductors, *Phys. Status Solidi B* **247**, 1498 (2010).
  - [2] D. R. Yakovlev, V. V. Pavlov, A. V. Rodina, R. V. Pisarev, J. Mund, W. Warkentin, and M. Bayer, Exciton spectroscopy of semiconductors by the method of optical harmonics generation (Review), *Phys. Solid State* **60**, 1471 (2018).
  - [3] M. Lafrentz, D. Brunne, A. V. Rodina, V. V. Pavlov, R. V. Pisarev, D. R. Yakovlev, A. Bakin, and M. Bayer, Second-harmonic generation spectroscopy of excitons in ZnO, *Phys. Rev. B* **88**, 235207 (2013).
  - [4] D. Brunne, M. Lafrentz, V. V. Pavlov, R. V. Pisarev, A. V. Rodina, D. R. Yakovlev, and M. Bayer, Electric field effect on optical harmonic generation at the exciton resonances in GaAs, *Phys. Rev. B* **92**, 085202 (2015).
  - [5] W. Warkentin, J. Mund, D. R. Yakovlev, V. V. Pavlov, R. V. Pisarev, A. V. Rodina, M. A. Semina, M. M. Glazov, E. L. Ivchenko, and M. Bayer, Third harmonic generation on exciton-polaritons in bulk semiconductors subject to a magnetic field, *Phys. Rev. B* **98**, 075204 (2018).
  - [6] J. Mund, D. Fröhlich, D. R. Yakovlev, and M. Bayer, High-resolution second harmonic generation spectroscopy with femtosecond laser pulses on excitons in Cu<sub>2</sub>O, *Phys. Rev. B* **98**, 085203 (2018).
  - [7] J. Mund, D. R. Yakovlev, M. A. Semina, and M. Bayer, Optical harmonic generation on the exciton-polariton in ZnSe, *Phys. Rev. B* **102**, 045203 (2020).
  - [8] A. Farenbruch, J. Mund, D. Fröhlich, D. R. Yakovlev, M. Bayer, M. A. Semina, and M. M. Glazov, Magneto-Stark and Zeeman effect as origin of second harmonic generation of excitons in Cu<sub>2</sub>O, *Phys. Rev. B* **101**, 115201 (2020).
  - [9] I. Sanger, D. R. Yakovlev, R. V. Pisarev, V. V. Pavlov, M. Bayer, G. Karczewski, T. Wojtowicz, and J. Kossut, Spin and Orbital Quantization of Electronic States as Origins of Second Harmonic Generation in Semiconductors, *Phys. Rev. Lett.* **96**, 117211 (2006).
  - [10] B. Kaminski, M. Lafrentz, R. V. Pisarev, D. R. Yakovlev, V. V. Pavlov, V. A. Lukoshkin, A. B. Henriques, G. Springholz, G. Bauer, E. Abramof, P. H. O. Rappl, and M. Bayer, Spin-Induced Optical Second Harmonic Generation in the Centrosymmetric Magnetic Semiconductors EuTe and EuSe, *Phys. Rev. Lett.* **103**, 057203 (2009).
  - [11] G. Wang, X. Marie, I. Gerber, T. Amand, D. Lagarde, L. Bouet, M. Vidal, A. Balocchi, and B. Urbaszek, Giant Enhancement of the Optical Second-Harmonic Emission of WSe<sub>2</sub> Monolayers

- by Laser Excitation at Exciton Resonances, *Phys. Rev. Lett.* **114**, 097403 (2015).
- [12] M. L. Trolle, Y.-C. Tsao, K. Pedersen, and T. G. Pedersen, Observation of excitonic resonances in the second harmonic spectrum of MoS<sub>2</sub>, *Phys. Rev. B* **92**, 161409(R) (2015).
- [13] M. M. Glazov, L. E. Golub, G. Wang, X. Marie, T. Amand, and B. Urbaszek, Intrinsic exciton-state mixing and nonlinear optical properties in transition metal dichalcogenide monolayers, *Phys. Rev. B* **95**, 035311 (2017).
- [14] J. Mund, A. Farenbruch, D. R. Yakovlev, A. A. Maksimov, A. Waag, and M. Bayer, Optical second and third harmonic generation on excitons in ZnSe/BeTe quantum wells, *Phys. Rev. B* **102**, 125433 (2020).
- [15] F. Bernardini, V. Fiorentini, and D. Vanderbilt, Spontaneous polarization and piezoelectric constants of III-V nitrides, *Phys. Rev. B* **56**, R10024 (1997).
- [16] T. Bretagnon, P. Lefebvre, T. Guillet, T. Taliercio, B. Gil, and C. Morhain, Barrier composition dependence of the internal electric field in ZnO/Zn<sub>1-x</sub>Mg<sub>x</sub>O quantum wells, *Appl. Phys. Lett.* **90**, 201912 (2007).
- [17] C. Klingshirn, ZnO: From basics towards applications, *Phys. Stat. Sol. B* **244**, 3027 (2007).
- [18] Ü. Özgür, Ya. I. Aliov, C. Liu, A. Teke, M. A. Reshchikov, S. Dogan, V. Avrutin, S.-J. Cho, and H. Morkoc, A comprehensive review of ZnO materials and devices, *J. Appl. Phys.* **98**, 041301 (2005).
- [19] M. Lafrentz, D. Brunne, B. Kaminski, V. V. Pavlov, A. V. Rodina, R. V. Pisarev, D. R. Yakovlev, A. Bakin, and M. Bayer, Magneto-Stark Effect of Excitons as the Origin of Second Harmonic Generation in ZnO, *Phys. Rev. Lett.* **110**, 116402 (2013).
- [20] X. Lu, H. Zhou, G. J. Salamo, Z. R. Tian, and M. Xiao, Generation of exciton-polaritons in ZnO microcrystallines using second-harmonic generation, *New J. Phys.* **14**, 073017 (2012).
- [21] A. Chaieb, A. Chari, and B. Sahraoui, Optical properties of ZnO nanocrystals embedded in PMMA, *Opt. Quantum Electron.* **46**, 39 (2014).
- [22] Y. Wang, L. Liao, T. Hu, S. Luo, L. Wu, J. Wang, Z. Zhang, W. Xie, L. Sun, A. V. Kavokin, X. Shen, and Z. Chen, Exciton-Polariton Fano Resonance Driven by Second Harmonic Generation, *Phys. Rev. Lett.* **118**, 063602 (2017).
- [23] J. C. Johnson, H. Yan, R. D. Schaller, P. B. Petersen, P. Yang, and R. J. Saykally, Near-field imaging of nonlinear optical mixing in single zinc oxide nanowires, *Nano Lett.* **2**, 279 (2002).
- [24] C. F. Zhang, Z. W. Dong, G. J. You, R. Y. Zhu, S. X. Qian, H. Deng, H. Cheng, and J. C. Wang, Femtosecond pulse excited two-photon photoluminescence and second harmonic generation in ZnO nanowires, *Appl. Phys. Lett.* **89**, 042117 (2006).
- [25] R. Prasanth, L. K. van Vugt, D. A. M. Vanmaekelbergh, and H. C. Gerritsen, Resonance enhancement of optical second harmonic generation in a ZnO nanowire, *Appl. Phys. Lett.* **88**, 181501 (2006).
- [26] K. Pedersen, C. Fisker, and T. G. Pedersen, Second-harmonic generation from ZnO nanowires, *Phys. Stat. Sol. C* **5**, 2671 (2008).
- [27] W. Chan, R. Barille, J. M. Nunzi, K. H. Tam, Y. H. Leung, W. K. Chan, and A. B. Djuricic, Second harmonic generation in zinc oxide nanorods, *Appl. Phys. B* **84**, 351 (2006).
- [28] Z. Gui, X. Wang, J. Liu, S. Yan, Y. Ding, Z. Wang, and Y. Hu, Chemical growth of ZnO nanorod arrays on textured nanoparticle nanoribbons and its second-harmonic generation performance, *J. Solid State Chem.* **179**, 1984 (2006).
- [29] S. W. Liu, H. J. Zhou, A. Ricca, R. Tian, and M. Xiao, Exciton-polariton Fano resonance driven by second harmonic generation, *Phys. Rev. B* **77**, 113311 (2008).
- [30] G.-Y. Zhuo, K.-J. Hsu, T.-Y. Su, N.-H. Huang, Y.-F. Chen, and S.-W. Chu, Effect of Lorentz local field for optical second order nonlinear susceptibility in ZnO nanorod, *J. Appl. Phys.* **111**, 103112 (2012).
- [31] J. Dai, J.-H. Zeng, S. Lan, X. Wan, and S.-L. Tie, Competition between second harmonic generation and two-photon-induced luminescence in single, double and multiple ZnO nanorods, *Opt. Express* **21**, 10025 (2013).
- [32] J. Dai, J.-H. Zeng, S. Lan, X. Wan, and S.-L. Tie, Negative slope for second harmonic generation observed at high excitation intensities in ZnO nanorods, *IEEE J. Quantum Electron.* **49**, 903 (2013).
- [33] M. C. Larciprete and M. Centini, Second harmonic generation from ZnO films and nanostructures, *Appl. Phys. Rev.* **2**, 031302 (2015).
- [34] J. Puls, S. Sadofev, P. Schäfer, and F. Henneberger, Optical in-plane anisotropy of ZnO/(Zn, Mg)O quantum wells grown on a-plane sapphire: implications for optical spin control, *Phys. Rev. B* **89**, 081301(R) (2014).
- [35] J. Puls, S. Sadofev, and F. Henneberger, Trions in ZnO quantum wells and verification of the valence band ordering, *Phys. Rev. B* **85**, 041307(R) (2012).
- [36] J. Kim, J. Puls, S. Sadofev, and F. Henneberger, Charged carrier spin dynamics in ZnO quantum wells and epilayers, *Phys. Rev. B* **93**, 045306 (2016).
- [37] I. A. Solovev, S. V. Poltavtsev, Yu. V. Kapitonov, I. A. Akimov, S. Sadofev, J. Puls, D. R. Yakovlev, and M. Bayer, Coherent dynamics of localized excitons and trions in ZnO/(Zn, Mg)O quantum wells studied by photon echoes, *Phys. Rev. B* **97**, 245406 (2018).
- [38] W. R. L. Lambrecht, A. V. Rodina, S. Limpijumng, B. Segall, and B. K. Meyer, Valence-band ordering and magneto-optic exciton fine structure in ZnO, *Phys. Rev. B* **65**, 075207 (2002).
- [39] A. Mang, K. Reimann, and St. Rübenacke, Band gaps, crystal-field splitting, spin-orbit coupling, and exciton binding energies in ZnO under hydrostatic pressure, *Solid State Commun.* **94**, 251 (1995).
- [40] B. K. Meyer, Band structure, in *Zinc Oxide. From Fundamental Properties Towards Novel Applications*, edited by C. F. Klingshirn, B. K. Meyer, A. Waag, A. Hoffmann, and J. Geurts (Springer-Verlag, Berlin, 2010), Chap. 4, pp. 77–94.
- [41] J. Wrzesinski and D. Fröhlich, Determination of electronic parameters of ZnO by nonlinear spectroscopy, *Solid State Commun.* **105**, 301 (1998).
- [42] T. Makino, Y. Segawa, M. Kawasaki, A. Ohtomo, R. Shiroki, K. Tamura, T. Yasuda, and H. Koinuma, Band gap engineering based on Mg<sub>1-x</sub>Zn<sub>x</sub>O and Cd<sub>y</sub>Zn<sub>1-y</sub>O ternary alloy films, *Appl. Phys. Lett.* **78**, 1237 (2001).
- [43] A. Ohtomo, K. Tamura, K. Saikusa, K. Takahashi, T. Makino, Y. Segawa, H. Koinuma, and M. Kawasaki, Single crystalline ZnO films grown on lattice-matched ScAlMgO<sub>4</sub> (0001) substrates, *Appl. Phys. Lett.* **75**, 2635 (1999).
- [44] K. Koike, K. Hama, I. Nakashima, G. Takada, K. Ogatab, S. Sasa, M. Inoue, and M. Yano, Molecular beam epitaxial growth of wide bandgap ZnMgO alloy films on (111)-oriented Si

- substrate toward UV-detector applications, *J. Crystal Growth* **278**, 288 (2005).
- [45] H. Morkoc and Ü. Özgür, *Zinc Oxide. Fundamentals, Materials and Device Technology* (Wiley-VCH Verlag, Weinheim, 2009).
- [46] G. Coli and K. K. Bajaj, Excitonic transitions in ZnO/MgZnO quantum well heterostructures, *Appl. Phys. Lett.* **78**, 2861 (2001).
- [47] L. Orphal, S. Kalusniak, O. Benson, and S. Sadofev, Tunable intersubband transitions in ZnO/ZnMgO multiple quantum wells in the mid infrared spectral range, *AIP Advances* **7**, 115309 (2017).
- [48] C. Morhain, T. Bretagnon, P. Lefebvre, X. Tang, P. Valvin, T. Guillet, B. Gil, T. Taliercio, M. Teisseire-Doninelli, B. Vinter, and C. Deparis, Internal electric field in wurtzite ZnO/Zn<sub>0.78</sub>Mg<sub>0.22</sub>O quantum wells, *Phys. Rev. B* **72**, 241305(R) (2005).
- [49] C. Xia, H. Zhang, J. An, S. Wei, and Y. Jia, Tunable built-in electric field and optical properties in wurtzite ZnO/MgZnO quantum wells, *Phys. Lett. A* **378**, 2251 (2014).
- [50] M. Yano, K. Hashimoto, K. Fujimoto, K. Koike, S. Sasa, M. Inoue, Y. Uetsuji, T. Ohnishi, and K. Inaba, Polarization-induced two-dimensional electron gas at Zn<sub>1-x</sub>Mg<sub>x</sub>O/ZnO heterointerface, *J. Cryst. Growth* **301–302**, 353 (2007).
- [51] T. Makino, Y. Segawa, A. Tsukazaki, A. Ohtomo, and M. Kawasaki, Photoexcitation screening of the built-in electric field in ZnO single quantum wells, *Appl. Phys. Lett.* **93**, 121907 (2008).
- [52] M. Leroux, N. Grandjean, J. Massies, B. Gil, P. Lefebvre, and P. Biegenwald, Barrier-width dependence of group-III nitrides quantum-well transition energies, *Phys. Rev. B* **60**, 1496 (1999).
- [53] T. Makino, Y. Segawa, M. Kawasaki, and H. Koinuma, Optical properties of excitons in ZnO-based quantum well heterostructures, *Semicond. Sci. Technol.* **20**, 78 (2005).
- [54] B. Gil, P. Lefebvre, T. Bretagnon, T. Guillet, J. A. Sans, T. Taliercio, and C. Morhain, Spin-exchange interaction in ZnO-based quantum wells, *Phys. Rev. B* **74**, 153302 (2006).
- [55] T. Makino, Y. Furuta, Y. Segawa, A. Tsukazaki, A. Ohtomo, Y. Hirayama, R. Shen, S. Takeyama, Y. Takagi, and M. Kawasaki, Magneto-optical study of n-type modulation-doped ZnO/Mg<sub>x</sub>Zn<sub>1-x</sub>O single quantum well structures, *Phys. Rev. B* **80**, 155333 (2009).
- [56] M. Fiebig, D. Fröhlich, and Ch. Pahlke-Lerch, Multiphoton polariton spectroscopy on ZnO, *Phys. Status Solidi B* **177**, 187 (1993).
- [57] H. D. Sun, Y. Segawa, T. Makino, C. H. Chia, M. Kawasaki, A. Ohtomo, K. Tamura, and H. Koinuma, Observation of biexciton emission in ZnO/ZnMgO multi-quantum wells, *Phys. Status Solidi B* **229**, 867 (2002).
- [58] J. M. Hvam, G. Blattner, M. Reuscher, and C. Klingshirn, The biexciton levels and nonlinear optical transitions in ZnO, *Phys. Status Solidi B* **118**, 179 (1983).
- [59] W. L. Bond, Measurement of the refractive indices of several crystals, *J. Appl. Phys.* **36**, 1674 (1965).
- [60] W. Weber, L. E. Golub, S. N. Danilov, J. Karch, C. Reitmaier, B. Wittmann, V. V. Bel'kov, E. L. Ivchenko, Z. D. Kvon, N. Q. Vinh, A. F. G. van der Meer, B. Mürdin, and S. D. Ganichev, Quantum ratchet effects induced by terahertz radiation in GaN-based two-dimensional structures, *Phys. Rev. B* **77**, 245304 (2008).
- [61] R. W. Boyd, *Nonlinear Optics* (Academic/Elsevier, Burlington, 2008).
- [62] H. Hardhienata, I. Priyadi, H. Alatas, M. D. Birowosuto, and P. Coquet, Bond model of second-harmonic generation in wurtzite ZnO(0002) structures with twin boundaries, *J. Opt. Soc. Am. B* **36**, 1127 (2019).
- [63] Y. Yan, M. M. Al-Jassim, M. F. Chrisholm, L. A. Boatner, S. J. Pennycook, and M. Oxley, [1100]/(1102) twin boundaries in wurtzite ZnO and group-III-nitrides, *Phys. Rev. B* **71**, 041309(R) (2005).